Article Open Access | Vita

Structural basis for heteromeric assembly and subthreshold activation of human M-channel

Yifei Wang[1,2,3#], Hui Yang[1,2,3#], Yannan Qu[1,2,3#], Junnan Li[4#], Xiao Li[1,2,3], Wenxin Hou[1], Kun Wu[1], Guanglei Xie[1,2,3], Xi Wang[1,2,3], Yangliang Ye[5], Huaiyu Yang[*4], Huaizong Shen[*1,2,3]

The M-channel, a heterotetrameric voltage-gated potassium channel formed by KCNQ2 and KCNQ3 subunits, critically regulates neuronal excitability, with dysfunction linked to epilepsy and developmental encephalopathies. Despite its physiological importance, structural mechanisms governing its unique heteromeric assembly and subthreshold gating have remained unresolved. We present cryo-EM structures of human M-channels, revealing unprecedented stoichiometric plasticity with all possible KCNQ2:KCNQ3 configurations (1:3 to 3:1) observed. Electrophysiologic studies of engineered concatemers show that these assemblies recapitulate native function. Structural analyses uncover that KCNQ3's voltage-sensing domain (VSD) adopts a more depolarized conformation than KCNQ2, explaining its signature subthreshold activation. Leveraging these insights, we developed CLM142, a structure-guided activator with 10-fold greater potency and specificity than the withdrawn drug retigabine. CLM142 enabled open-state structure determination, revealing how PIP_2 binding couples VSD movement to pore opening. Our work provides a framework for understanding the M-channel's unique assembly and distinctive physiology, revealing critical insights into related disease mechanisms and targeted therapeutics design.

https://doi.org/10.15302/vita.2026.05.0032

INTRODUCTION

The M-channel, a heteromeric voltage-gated potassium (K_v) channel composed of KCNQ2 and KCNQ3 subunits[1-3], governs neuronal excitability by generating a slowly activating, non-inactivating potassium current (I_M) that dampens repetitive firing[2, 4-6]. First identified in sympathetic neurons for its suppression by muscarinic acetylcholine receptor signaling (hence "M"-channel)[4], it is now recognized as a master regulator of action potential threshold and spike-frequency adaptation across the central and peripheral nervous systems[6-12]. The molecular identity of I_M was established with the cloning of *KCNQ2* and *KCNQ3*[1, 2, 13-16], which form heteromeric channels with biophysical properties precisely matching native M-currents — distinct from their homomeric counterparts[1-3, 17]. Dysfunction of these subunits underlies a spectrum of severe neurological disorders, including benign familial neonatal seizures (BFNS)[3, 5, 13-15, 18-27], developmental epileptic encephalopathies (DEE7)[22, 28-31], and autism-associated phenotypes[32-35], underscoring their critical physiological and therapeutic relevance[36].

Despite decades of research, fundamental questions regarding the M-channel's architecture and gating mechanisms remain unresolved[34, 37]. A central controversy concerns its heteromeric stoichiometry[34]: while biochemical and functional studies suggested a 2:2 (KCNQ2:KCNQ3) assembly[2, 38], others proposed variable or asymmetric arrangements[39, 40]. This uncertainty has obscured how subunit composition dictates the channel's unique subthreshold activation — a hallmark feature enabling I_M to stabilize resting membrane potentials[2, 4, 6]. Although recent structures of homomeric KCNQ channels have revealed their canonical architecture[37, 41-46], the absence of heteromeric M-channel structures has precluded mechanistic understanding of its distinct gating properties and subunit cooperativity[34, 47, 48]. Resolving these questions is critical for both ion channel biology and drug discovery, particularly given the M-channel's validation as a target for epilepsy and neuropsychiatric disorders[47, 49-52].

Therapeutic targeting of the M-channel has faced significant hurdles[49, 53]. Retigabine, the first-in-class M-channel activator approved for refractory epilepsy, was withdrawn due to several adverse effects (*e.g.*, bladder toxicity and retinal discoloration) linked to its activity across multiple KCNQ subtypes or metabolism in the human body[51, 52, 54-60]. Developing subtype-selective activators requires precise structural insights into the heteromeric channel's drug-binding sites and activation mechanisms — a goal hindered by the lack of M-channel structures.

Here, we resolve these longstanding questions through cryo-electron microscopy (cryo-EM) structures of the human M-channel in multiple functional states. Our findings reveal unexpected stoichiometric flexibility in KCNQ2:KCNQ3 assemblies and identify a markedly depolarized conformation of the voltage-sensing domain (VSD) in KCNQ3 compared to KCNQ2, providing the first structural explanation for the channel's characteristic subthreshold activation. Electrophysiological characterizations of engineered concatemers and chimeric constructs corroborate these structural insights. Leveraging this knowledge, we developed CLM142 (**1**), a potent and

---

1. Zhejiang Key Laboratory of Structural Biology, School of Life Sciences, Westlake University, Hangzhou, Zhejiang, China. 2. Westlake Laboratory of Life Sciences and Biomedicine, Hangzhou, Zhejiang, China. 3. Westlake Institute for Advanced Study, Hangzhou, Zhejiang, China. 4. Shanghai Key Laboratory of Regulatory Biology, Institute of Biomedical Sciences and School of Life Sciences, East China Normal University, Shanghai, China. 5. Suzhou Institute of Materia Medica, Suzhou, Jiangsu, China. [#]These authors contributed equally *Correspondence: Huaiyu Yang (hyyang@bio.ecnu.edu.cn), Huaizong Shen (shenhuaizong@westlake.edu.cn)

Received: December 4, 2025; Accepted: May 11, 2026; Published: May 27, 2026

selective M-channel activator that facilitated determination of the open-state structure. Our work not only elucidates fundamental principles of M-channel assembly and gating but also establishes a framework for structure-guided development of targeted therapies.

RESULTS

Structure of the human M-channel reveals unexpected stoichiometric plasticity

We determined cryo-EM structures of the human M-channel using wild-type (WT) of both KCNQ2/KCNQ3 heteromers and engineered constructs where flexible N- and C-terminal regions and the disordered loop between HA and HB helices were removed to improve biochemical stability (Fig. 1a; Supplementary Figs. S1–S11 and Tables S1–S5). The functional integrity of the engineered constructs was confirmed through electrophysiological recordings. This approach enabled us to resolve four distinct structural states: the WT M-channel (Fig. 1a), the engineered construct in the *apo* state (*apo* M-channel; Supplementary Fig. S3a), the construct

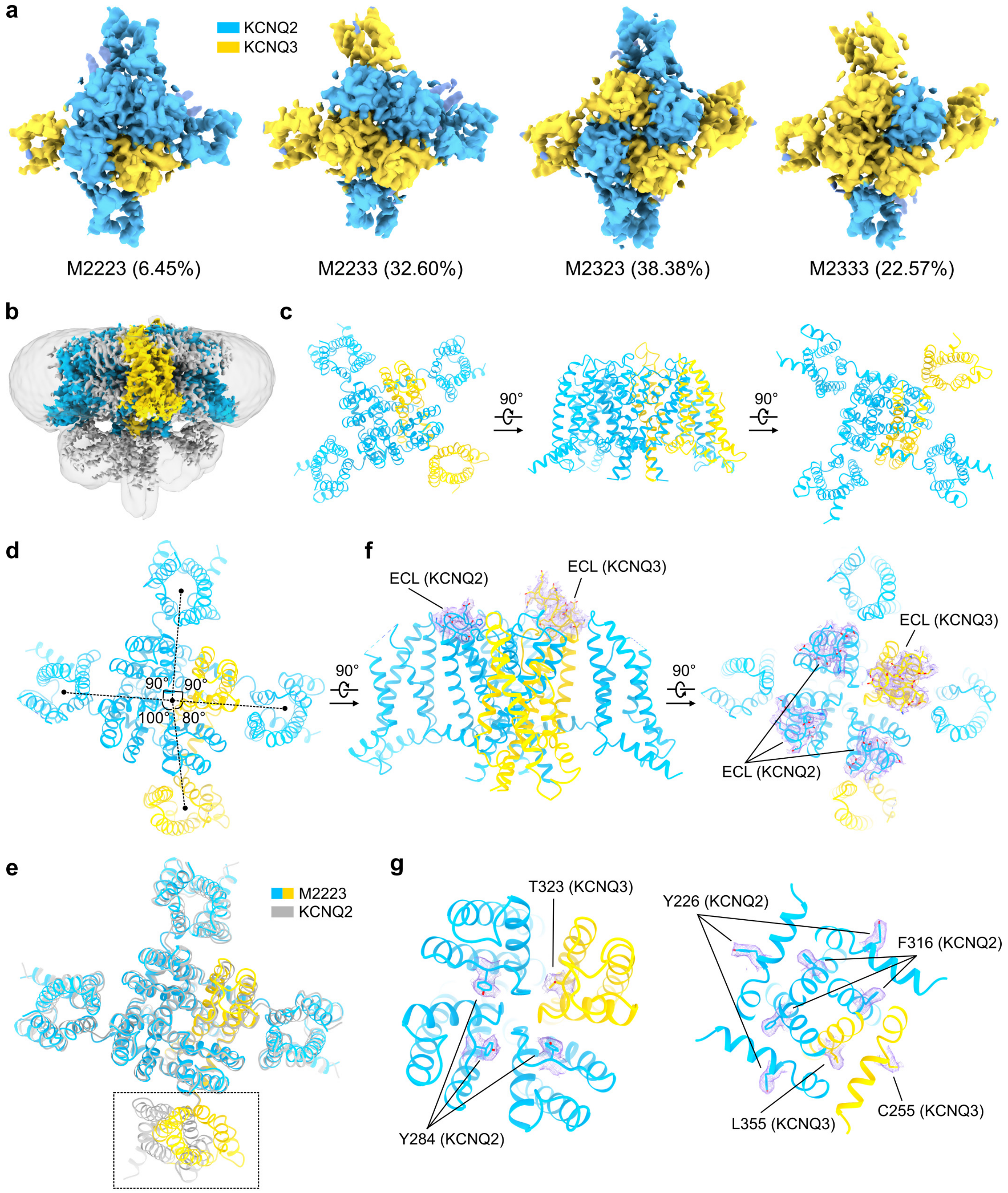

Fig. 1 Structural architecture and stoichiometric flexibility of the human M-channel. a Cryo-EM reconstructions of the four distinct M-channel stoichiometries (M2223, M2233, M2323, M2333) with their relative abundances indicated. KCNQ2 and KCNQ3 subunits are colored blue and yellow, respectively. **b** Representative cryo-EM density map for the *apo* M2223 configuration. **c** Atomic model corresponding to the map in **b**, displayed in three orthogonal views. **d** Differential positioning of the VSDs relative to the PD in KCNQ2 vs KCNQ3, illustrated by a comparison of their tilt angles. **e** Structural alignment of the *apo* M2223 and KCNQ2 homotetramer highlighting the differential positioning of their VSDs. **f** ECL of KCNQ3 is markedly longer than that of KCNQ2, resulting in a pronounced difference in cryo-EM density. **g** High-resolution features that enable unambiguous subunit discrimination, including characteristic side chain densities for Y284, Y226, and F316 in KCNQ2 and T323, C255, and L355 in KCNQ3 within the PD. All structure figures are generated in ChimeraX[86].

bound to the activator CLM142 (CLM142-bound M-channel; Supplementary Fig. S3b), and the construct in the open state stabilized by both CLM142 and PIP_2 (open-state M-channel; Supplementary Fig. S3c).

All resolved structures adopted the canonical voltage-gated K^+ channel architecture, with four VSDs surrounding a central pore domain (PD; Fig. 1a–c)[61]. However, unlike homomeric channels, the M-channel's central pore and VSDs are formed by asymmetric arrangements of KCNQ2 and KCNQ3 subunits[37, 41-44, 46]. The local resolution of the cytosolic domains, crucial for the tetrameric assembly[62, 63], was poor and precluded reliable modeling. Three key structural features enabled unambiguous discrimination between subunits: first, the VSD of KCNQ3 adopts a distinct orientation relative to the central pore compared to KCNQ2 (Fig. 1d, e); second, KCNQ3 possesses a significantly longer extracellular loop (ECL) which yields a pronounced density difference (Fig. 1f; Supplementary Figs. S1, S12); and third, the high resolution (~2.8 Å) of the central pore region allowed discrimination of non-conserved residues, including Y284 in KCNQ2 vs T323 in KCNQ3, F316 in KCNQ2 vs L355 in KCNQ3, and Y226 in KCNQ2 vs C255 in KCNQ3 (Fig. 1g; Supplementary Fig. S1).

Analysis of these preparations revealed that the M-channel exists in four distinct stoichiometric configurations (Fig. 1a; Supplementary Fig. S3). These include a 3:1 KCNQ2:KCNQ3 assembly (M2223), two 2:2 assemblies with either adjacent (M2233) or alternating (M2323) subunit arrangements, and a 1:3 assembly (M2333). Intriguingly, the relative proportions of these assemblies varied significantly between preparations. Under our standard co-expression conditions for WT subunits, the KCNQ2-rich M2223 configuration was the least prevalent (6.45%), indicating an inherent assembly preference under these conditions that favors incorporation of KCNQ3. This resulted in a population dominated by the balanced 2:2 stoichiometries (M2323, 38.38%; M2233, 32.6%) and the KCNQ3-rich M2333 configuration (22.57%).

In contrast, engineered constructs exhibited a pronounced redistribution, with the M2223 configuration becoming dominant (53.2% in *apo* M-channel) (Supplementary Fig. S3), correlating with higher expression levels of KCNQ2 relative to KCNQ3 (Supplementary Fig. S2b). This shift likely reflects a combination of altered expression levels and the enhanced biochemical stabilities of the truncated subunits compared to their WT counterparts. This stoichiometric plasticity was further quantified through systematic transfection experiments using defined ratios of KCNQ2-GFP and KCNQ3 plasmids (1:1, 1:4, and 1:9). By measuring the ratio of peak GFP fluorescence (reporting KCNQ2 incorporation) to the total UV absorbance of the purified tetramers (reporting total protein yield), we observed a progressive decrease in the relative KCNQ2 content (146, 128, and 54 mV per mAu, respectively) as KCNQ3 availability increased (Supplementary Fig. S13; see Materials and Methods for detailed protocols). Collectively, these data demonstrate that stoichiometric flexibility is an inherent property of M-channel assembly, where the final population distribution is determined by the relative availability and biochemical stability of the subunits within the expression system.

The high-resolution structure enables precise structural alignment of the subunit interface (S5 and S6 helices) of KCNQ2 and KCNQ3, revealing an exceptional degree of conservation in both sequence (> 90% similarity) and tertiary structure (RMSD = 0.437 Å; Supplementary Fig. S14). This near-perfect structural compatibility explains the M-channel's remarkable stoichiometric plasticity, permitting all combinatorially possible configurations (M2223, M2233, M2323, and M2333) to assemble through favorable structural compatibility at the subunit interfaces.

Concatemeric constructs of KCNQ2 and KCNQ3 recapitulate electrophysiological properties of the WT M-channel

To validate the physiological relevance of the observed stoichiometric assemblies, we engineered concatemers with defined subunit ratios matching our structural findings: 3:1 (M2223), two distinct 2:2 arrangements (M2323 and M2233), and 1:3 (M2333) (Fig. 2a). Fluorescence size-exclusion chromatography confirmed that these concatemeric constructs form stable tetrameric assemblies with elution profiles matching the WT M-channel (Supplementary Fig. S15). These designs enabled precise control over subunit composition while maintaining native inter-domain connectivity.

We performed comprehensive electrophysiological characterization using both whole-cell and single-channel recordings (Fig. 2). WT M-channels (co-expressed KCNQ2/KCNQ3) served as functional benchmarks (Fig. 2b–d), while KCNQ2 homomers provided baseline references for homomeric channel properties. Whole-cell recording results demonstrated that all four concatemer configurations produced current-voltage (I-V) relationships superimposable with WT M-channels, with activation thresholds consistently shifted toward hyperpolarized potentials compared to KCNQ2 homomers (Fig. 2c, d). Quantitative analysis revealed that each concatemer exhibited half-maximal activation voltages ($V_{1/2}$) statistically indistinguishable from WT M-channels ($P > 0.05$) yet significantly more hyperpolarized than KCNQ2 homomers ($P < 0.001$), recapitulating the hallmark subthreshold activation profile of native M-channels[2]. To further evaluate their steady-state and kinetic properties, we estimated the apparent gating charges and measured the voltage-driven activation kinetics (Supplementary Fig. S16). The apparent gating charges showed no significant differences across the WT M-channel, the four concatemers, and the KCNQ2 homomer. Furthermore, despite structural variations in their voltage-sensing domains, all concatemers exhibited macroscopic activation kinetics that closely matched the WT M-channel, which were significantly faster than those of homomeric KCNQ2.

Single-channel analyses provided mechanistic corroboration at the molecular level. All concatemer variants displayed unitary current amplitudes (Fig. 2e), single-channel conductance (Fig. 2f), and open probabilities (Fig. 2g) matching WT M-channels within experimental error ($P > 0.05$ for all parameters across constructs). To uncover potential fine-scale kinetic distinctions among the different stoichiometric assemblies, we analyzed the dwell-time distributions for both open and closed states (Supplementary Fig. S17). Both closed and open events were typically best fit with a mixture of two exponential distributions. While we observed subtle variations in microscopic kinetics (*e.g.*, the bimodal open-time distributions showed varying degrees of dispersion among configurations), the distinct concatemers shared broadly similar overall dwell-time profiles with the WT channel. This functional equivalence across distinct stoichiometries demonstrates that each assembly configuration faithfully reproduces the fundamental biophysical properties of native M-channels[17].

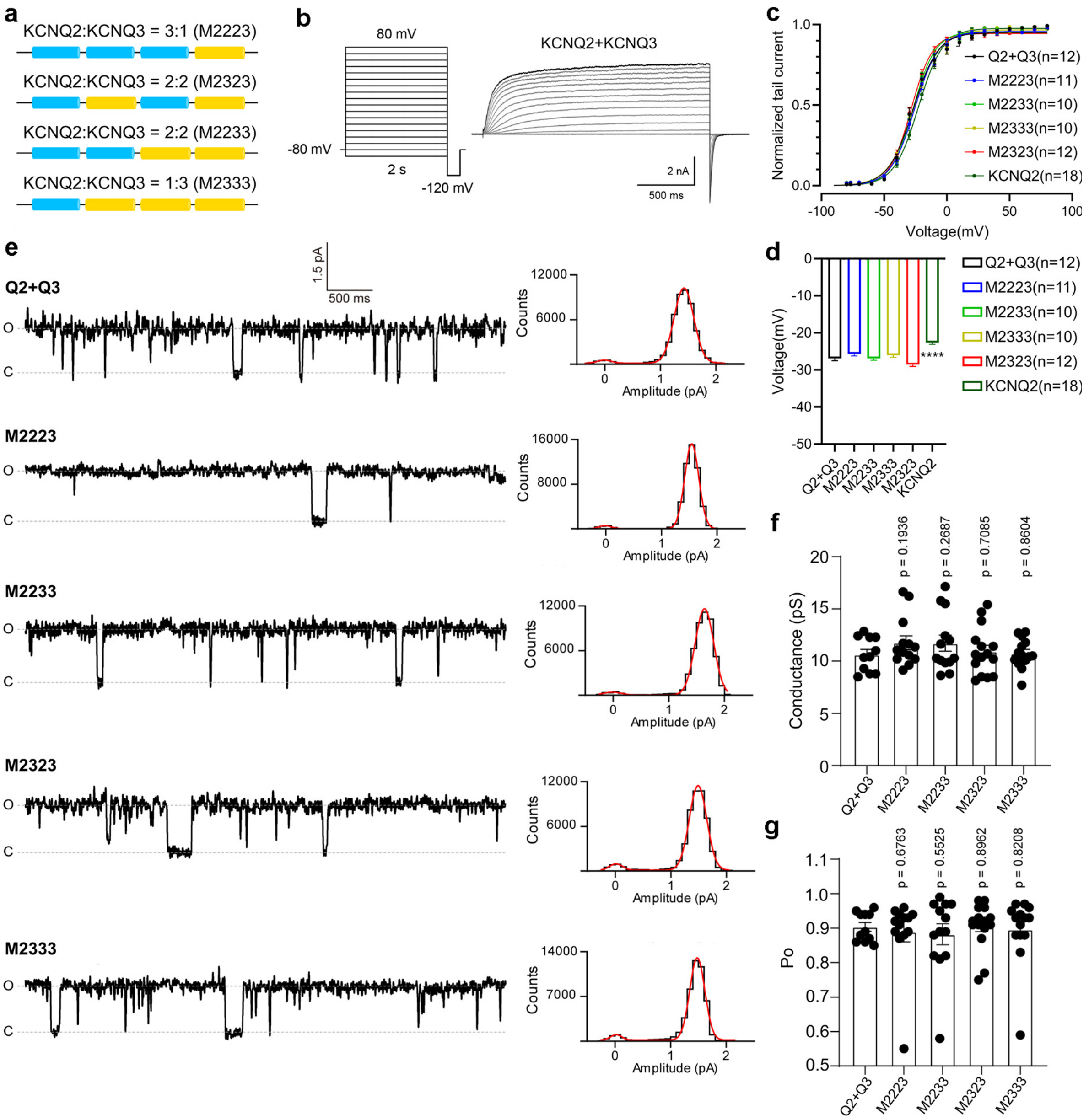

Fig. 2 Concatemeric KCNQ2/KCNQ3 channels recapitulate WT M-channel properties. **a** Schematic representations of the engineered concatemeric constructs with defined KCNQ2 (blue) and KCNQ3 (yellow) subunit stoichiometries. **b** Left: Whole-cell recording protocol. Right: Representative current traces from WT M-channels (KCNQ2/KCNQ3 co-expression). Currents were elicited by 2 s depolarizing steps from −90 to +80 mV in 10 mV increments from a holding potential of −80 mV, followed by a −120 mV tail pulse (250 ms). **c** Whole-cell current-voltage (I-V) relationships for the indicated concatemers and WT channels. **d** Half-maximal activation voltages ($V_{1/2}$) show that all concatemeric channels exhibit significantly hyperpolarized activation compared to KCNQ2 homomers, recapitulating the WT M-channel phenotype. **e** Representative single-channel current traces for each concatemeric variant. Scale bars: 1.5 pA (vertical), 500 ms (horizontal). **f** Summary of unitary current amplitudes from single-channel recordings. **g** Summary of open probability (P_o) for each concatemeric channel. Data in **c**, **d**, **f**, and **g** are presented as mean ± SEM (n ≥ 10). Statistical significance was determined by an unpaired two-tailed Student's *t*-test ($^{*}P < 0.05$, $^{**}P < 0.01$, $^{***}P < 0.001$, $^{****}P < 0.0001$).

The KCNQ3 VSD confers hyperpolarized activation kinetics

The M-channel's physiological importance stems from its unique ability to activate at subthreshold membrane potentials, a property critical for regulating neuronal excitability[2,4,6]. Despite its functional significance, the structural basis for this distinctive gating behavior has remained elusive.

In voltage-gated ion channels, VSD activation is defined by the positions of S4 arginine residues (R1–R6) relative to the charge transfer center, which comprises a conserved phenylalanine (F137 in KCNQ2; F167 in KCNQ3) flanked by two acidic residues (E130/E140 in KCNQ2; E160/E170 in KCNQ3; Fig. 3a; Supplementary Fig. S1)[64]. Comparative structural analysis of the *apo* M-channel revealed striking differences between subunits: while R4 (R207) in KCNQ2 forms cation–π interactions with F137 and sits slightly above it, KCNQ3's R4 (R236) resides farther above F167, with R5 (R239) instead forming the cation–π interaction below (Fig. 3a). This conformational disparity suggests that the KCNQ3 VSD adopts a more activated state than the KCNQ2 VSD, indicating that the KCNQ3 subunit is more easily activated at hyperpolarized membrane potentials. These structural observations provide a plausible mechanism for the M-channel's hyperpolarized activation threshold relative to KCNQ2 homomers.

To test whether KCNQ3's VSD drives subthreshold activation, we engineered chimeric constructs by swapping VSDs between subunits: VSD_2-PD_3 (KCNQ2 VSD + KCNQ3 pore) and VSD_3-PD_2 (KCNQ3 VSD + KCNQ2 pore) (Fig. 3b; Supplementary Fig. S1). Electrophysiological characterization revealed

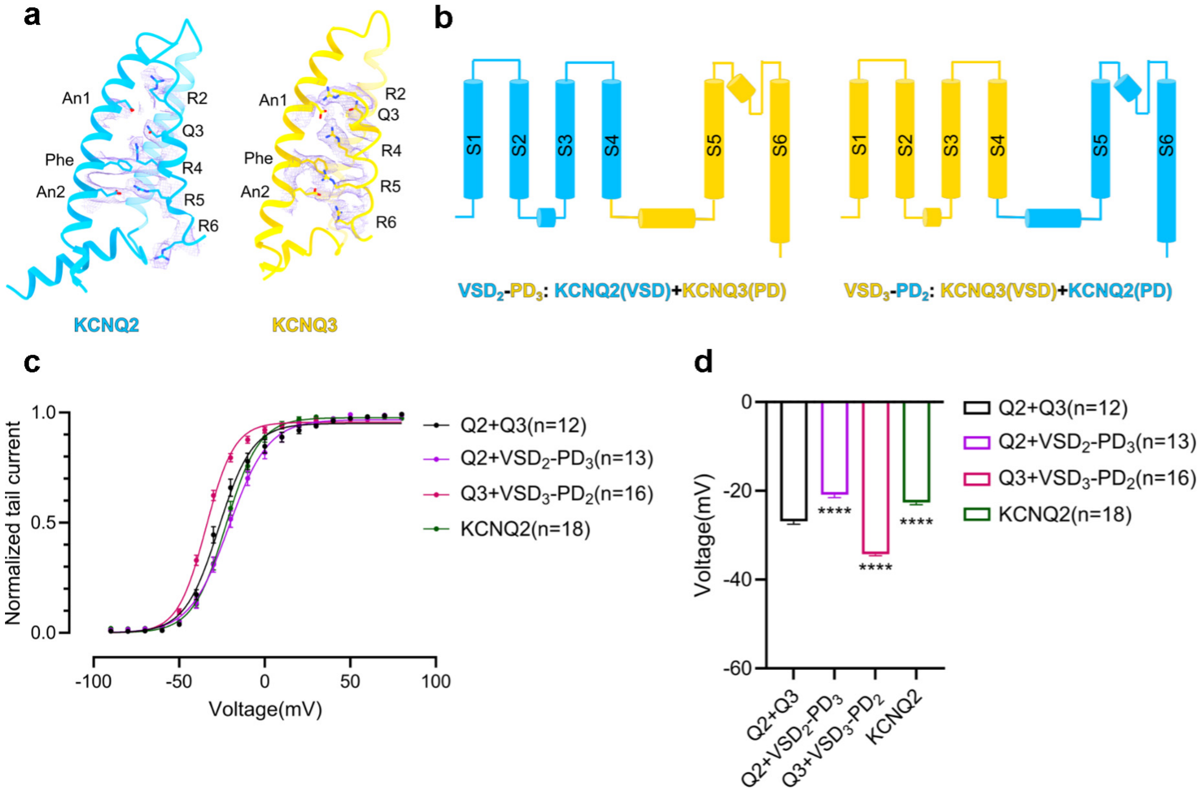

Fig. 3 The KCNQ3 VSD confers hyperpolarized activation kinetics. a Structural comparison of the VSDs from KCNQ2 (blue) and KCNQ3 (yellow) in the *apo* M2223 structure. The relative positions of the S4 arginine residues (R2–R6) to the charge transfer center on S2 reveal that the KCNQ3 VSD adopts a more depolarized conformation. **b** Design strategy for chimeric constructs in which the VSDs were swapped between KCNQ2 and KCNQ3, creating VSD$_3$-PD$_2$ and VSD$_2$-PD$_3$ subunits. **c** Whole-cell current-voltage (I-V) relationships for WT and chimeric channels. **d** Half-maximal activation voltages (V$_{1/2}$) show that channels incorporating the KCNQ3 VSD (VSD$_3$-PD$_2$ + KCNQ3) activate at more hyperpolarized potentials, while channels with the KCNQ2 VSD (VSD$_2$-PD$_3$ + KCNQ2) exhibit depolarized activation akin to KCNQ2 homomers. Data are presented as mean ± SEM (n ≥ 12). Statistical significance was determined by an unpaired two-tailed Student's *t*-test (*****P* < 0.0001).

that channels containing only KCNQ2 VSDs (VSD$_2$-PD$_3$ + KCNQ2) exhibited activation thresholds similar to KCNQ2 homomers (Fig. 3c, d). Conversely, channels with exclusively KCNQ3 VSDs (VSD$_3$-PD$_2$ + KCNQ3) activated at even more hyperpolarized potentials than WT M-channels. This finding is consistent with the hyperpolarized activation profile we observed for the homomeric KCNQ3 channel (V$_{1/2}$ = −33.49 ± 1.87 mV; Supplementary Fig. S18), with the activation threshold of the native heteromer situated at an intermediate level between these two extremes (Fig. 3c, d). These results definitively establish that KCNQ3's VSD is both necessary and sufficient for the M-channel's subthreshold activation phenotype.

Identification and characterization of the selective M-channel activator CLM142

The withdrawal of retigabine (Fig. 4b), the first clinically approved M-channel activator, partially due to off-target effects across KCNQ subtypes (Supplementary Fig. S19), highlighted the critical need for selective therapeutics[47, 49, 51, 52, 54-59]. Through structure-guided drug design informed by both the M-channel architecture and retigabine's activation mechanism, we developed CLM142, a next-generation activator identified via an integrated virtual screening and electrophysiological validation approach (Fig. 4a; Supplementary Fig. S20; see Materials and Methods for detailed screening procedures).

CLM142 features three key structural elements: (i) a fluorophenyl group linked via (ii) an amide bond to (iii) an indazole core with cyclopropyl and ethynyl substitutions (Fig. 4a). These strategic modifications yielded significant pharmacological improvements, demonstrating a 10-fold greater potency than retigabine on human M-channel (EC$_{50}$ = 0.19 ± 0.09 µM vs 2.16 ± 0.15 µM for G-V curve shifts) (Fig. 4c–e; Supplementary Fig. S21a). At 1 µM concentration, CLM142 produced a ΔV$_{1/2}$ shift of −32.49 ± 1.64 mV (Fig. 4c, d) and significantly modulated channel kinetics, accelerating activation (118.09 ± 9.21 ms vs 172.09 ± 17.19 ms at 0 mV; Supplementary Fig. S21b) while slowing deactivation (126.54 ± 12.98 ms vs 19.51 ± 2.72 ms; Supplementary Fig. S21c). Moreover, CLM142 achieves a remarkable subtype specificity (Fig. 4f; Supplementary Fig. S22). Even at a high concentration of 10 µM, CLM142 exerted negligible effects on KCNQ1 activation. For KCNQ4 and KCNQ5, noticeable but minimal hyperpolarizing shifts (~10 mV) were only observed at 10 µM, a concentration over 50 times higher than its EC$_{50}$ for the M-channel. At 1 µM concentration, where CLM142 produced a massive activation shift for the M-channel, the compound showed negligible effects on these other subtypes. These properties establish CLM142 as a promising therapeutic candidate, combining submicromolar potency with the precise subtype selectivity required to avoid the historical pitfalls of retigabine.

Molecular mechanism for the potent activation of CLM142 on human M-channel

To elucidate its mechanism of action, we determined the cryo-EM structure of CLM142-bound M-channel at 3.1 Å resolution (Fig. 5a, b; Supplementary Figs. S3, S4, and S10). CLM142 occupies the inter-subunit pocket between S5 and S6 helices (Fig. 5c) — the canonical activator binding site shared with

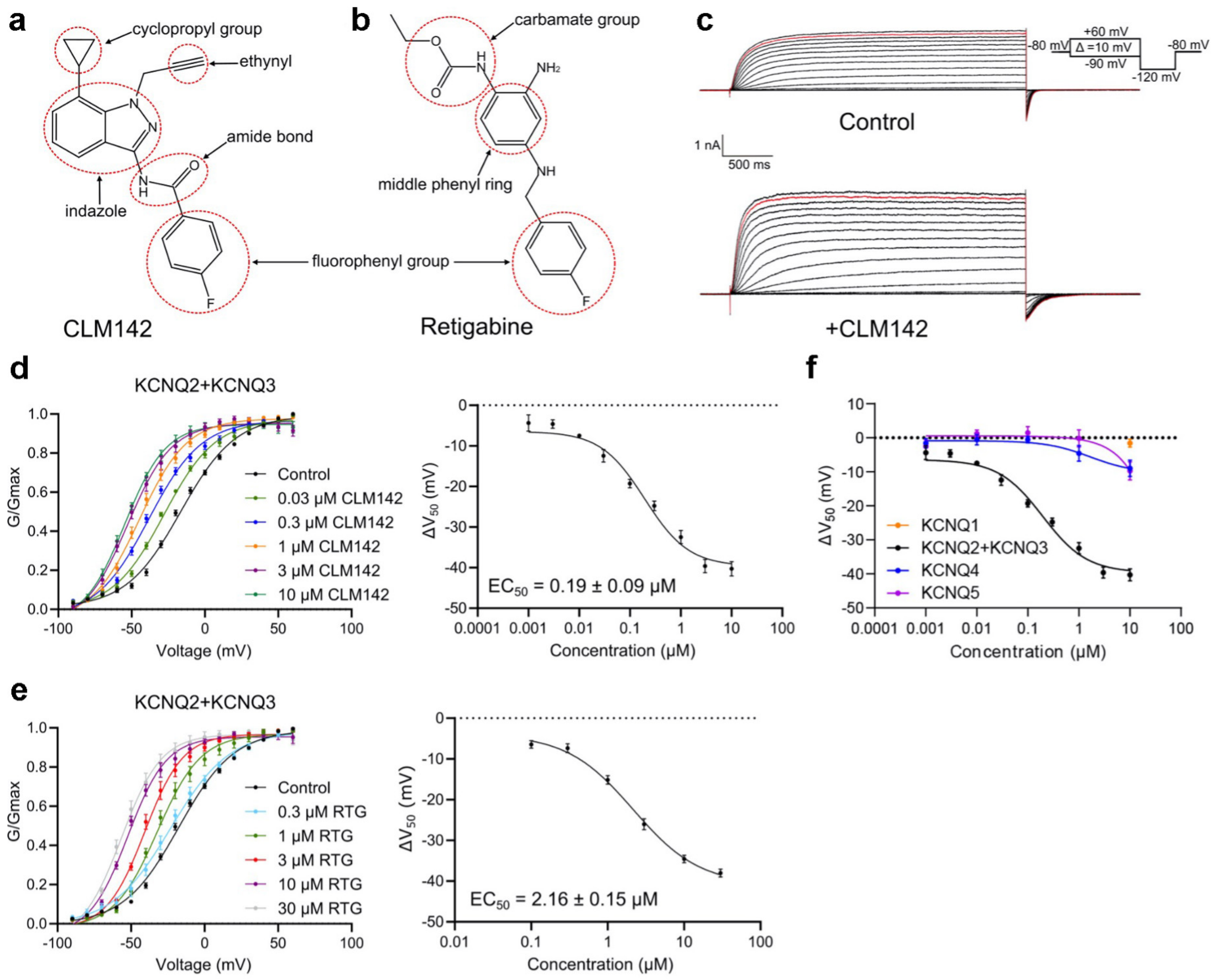

Fig. 4 CLM142 is a potent and selective M-channel activator with superior properties to retigabine. **a** Chemical structure of the novel M-channel activator CLM142, with key functional groups labeled. **b** Chemical structure of the canonical M-channel activator retigabine for comparison. **c** Representative whole-cell current traces from M-channels showing potent activation by 1 μM CLM142. **d** Left: Concentration-dependent conductance-voltage (G-V) relationships for CLM142. Right: Summary of the concentration-dependent hyperpolarizing shifts in the half-maximal activation voltage ($\Delta V_{1/2}$) induced by CLM142. **e** Left: Concentration-dependent G-V relationships for retigabine. Right: Summary of the $\Delta V_{1/2}$ shifts induced by retigabine. CLM142 exhibits an approximate 10-fold greater potency (EC_{50} = 0.19 ± 0.09 μM) than retigabine (EC_{50} = 2.16 ± 0.15 μM). **f** Quantitative comparison of the $\Delta V_{1/2}$ induced by CLM142 on human M-channel vs KCNQ1, KCNQ4, and KCNQ5, demonstrating CLM142's high selectivity for the neuronal M-channel. Data in **d**–**f** are presented as mean ± SEM (n ≥ 5).

retigabine (Supplementary Fig. S19) — but establishes a unique interaction network through its distinct chemical architecture (Fig. 5d)[37, 43]. The compound binds in a characteristic orientation where its fluorophenyl tail extends intracellularly while the cyclopropyl/ethynyl moieties project extracellularly (Fig. 5d). Within this pocket, the amide carbonyl forms a crucial hydrogen bond with S303/S342 on S6, while the central indazole core engages in robust π–π stacking with the highly conserved W236/W265 on S5. Simultaneously, the cyclopropyl/ethynyl groups are sequestered within a hydrophobic pocket formed by F240/F269 on S5 and L299/L338-F305/F344 on S6, while the fluorophenyl group makes complementary van der Waals contacts with F304/F343, L221/L250, V225/I254 and L312/L352. This sophisticated interplay of directional hydrogen bonding and extensive hydrophobic complementarity synergistically enables CLM142 to bind and activate the M-channel.

Comparative analysis with retigabine and Ebio2 reveals several distinct structural advantages that provide a rationale for the 10-fold increase in potency exhibited by CLM142 (Supplementary Fig. S23). Most notably, the rigid indazole-amide scaffold of CLM142 directs its extended fluorophenyl tail to anchor into a deep hydrophobic sub-pocket beneath the primary binding site. This critical anchoring space remains completely unutilized by the more flexible retigabine molecule. Furthermore, the highly aromatic indazole ring significantly strengthens the π–π stacking interaction with the S5 tryptophan compared to the simpler triaminobenzene core of earlier activators. This interaction also explains the improved subtype selectivity of CLM142. In KCNQ1, this critical tryptophan is replaced by a leucine residue (L266), which effectively abolishes the CLM142 binding site and explains the lack of drug activity on that subtype.

Despite these significant structural modifications and the superior shape complementarity of its binding pose, CLM142 activates the channel through a mechanism reminiscent of retigabine. The compound promotes PD opening by inducing a clockwise rotation of the S5 and S6 helices when viewed from the intracellular side (Fig. 5d)[37, 43, 65]. This mechanical movement is evidenced by the significant displacement of W236 in KCNQ2 and W265 in KCNQ3 (Fig. 5d), confirming that both activators share a common downstream pathway for gate opening regardless of their distinct chemical geometries. This sophisticated interplay of directional hydrogen bonding and deep hydrophobic anchoring synergistically enables CLM142 to stabilize the open state with high potency and

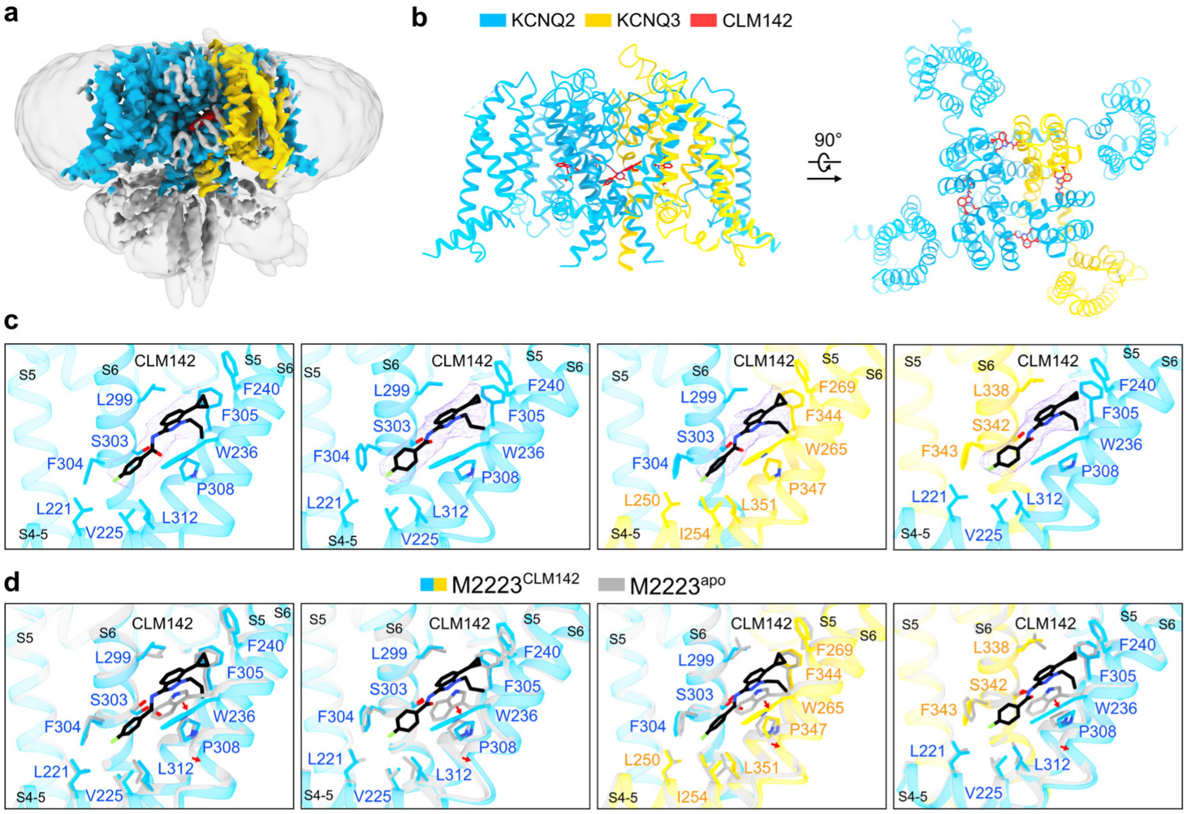

Fig. 5 Structural basis for potent activation of the M-channel by CLM142. a Cryo-EM density map of the CLM142-bound M2223 complex. **b** Atomic model of the CLM142-bound M2223 complex, displayed in two orthogonal views. **c** Detailed architecture of the CLM142 binding pocket, located at the interface between the S5 and S6 helices of adjacent subunits. Four drug molecules (black) are present per tetramer. CLM142 forms extensive hydrophobic and π–π stacking interactions with surrounding residues, with the atomic model showing excellent agreement with the high-resolution cryo-EM density. **d** Activation mechanism. Binding of CLM142 induces a displacement of the conserved tryptophan (W236 in KCNQ2; W265 in KCNQ3) and a clockwise rotation of the S5 helices (intracellular view), which favors the activation of the PD.

specificity.

Open-state structure of M-channel reveals its activation mechanism

To elucidate the structural basis of M-channel activation, we determined the open-state structure of the human M-channel (open-state M-channel) in complex with CLM142 and PIP_2 (Fig. 6a, b; Supplementary Figs. S3, S4, and S11). While maintaining the four CLM142 molecules bound between S5-S6 helices observed in the closed state (Fig. 6b), the intracellular gate formed by L318 in KCNQ2 (L357 in KCNQ3) of the open structure undergoes significant dilation, expanding from less than 1 Å to over 2 Å in radius (Fig. 6c, d). This pore opening results from a coordinated clockwise rotation of S6 helices (viewed intracellularly) initiated at the conserved G313 in KCNQ2 (G352 in KCNQ3) within the GSG motif, coupled with outward displacement of the gate-forming leucine side chains (L318/L357) (Fig. 6e; Supplementary Figs. S1, S24). These movements align with established activation mechanisms in voltage-gated channels[43, 65].

The structure captures four weak densities beneath the VSDs, which we assign as PIP_2 based on three lines of evidence (Fig. 6f): (i) their exclusive appearance in PIP_2-supplemented samples, (ii) the open conformation's dependence on PIP_2 in KCNQ channels[8, 48, 66-68], and (iii) congruence with PIP_2 binding sites in other open-state KCNQ structures[37, 42, 44-46, 69]. These lipids engage multiple positively charged residues, including R87/R117 and R89/R119 in the VSD, R213/R242 and R214/R243 in the S4-S5 linker, and K327/K366 in the extended S6 helix through electrostatic interactions, consistent with previous studies[42, 44-46]. These interactions support an activation mechanism whereby PIP_2 binding to this basic residue-rich interface couples S4 movement to S6 displacement, facilitating gate opening. The pivotal role of the conserved GSG motif (G313/G352) as a gating hinge is underscored by its position at the initiation point of these conformational changes (Supplementary Fig. S1).

DISCUSSION

Our systematic structural and functional characterization of the human M-channel resolves several long-standing questions in the field while providing new insights into its physiological regulation, pathophysiological mechanism and therapeutic targeting (Supplementary Fig. S25).

Our cryo-EM structures reveal unexpected stoichiometric plasticity in the M-channel, which can adopt all possible KCNQ2:KCNQ3 configurations (M2223, M2233, M2323, and M2333). This remarkable structural flexibility likely stems from the high degree of sequence conservation and structural similarity between KCNQ2 and KCNQ3 subunits. The relative abundance of these assemblies varies across preparations, correlating with differential expression levels of KCNQ2 and KCNQ3. This structural flexibility resolves previous conflicting reports about M-channel composition, where some studies proposed fixed 1:1 stoichiometry while others suggested variable ratios[2, 38-40]. The discrepancy likely stems from unaccounted variations in subunit expression levels across experimental systems.

This plasticity may represent an important endogenous mechanism for tuning neuronal excitability, particularly given

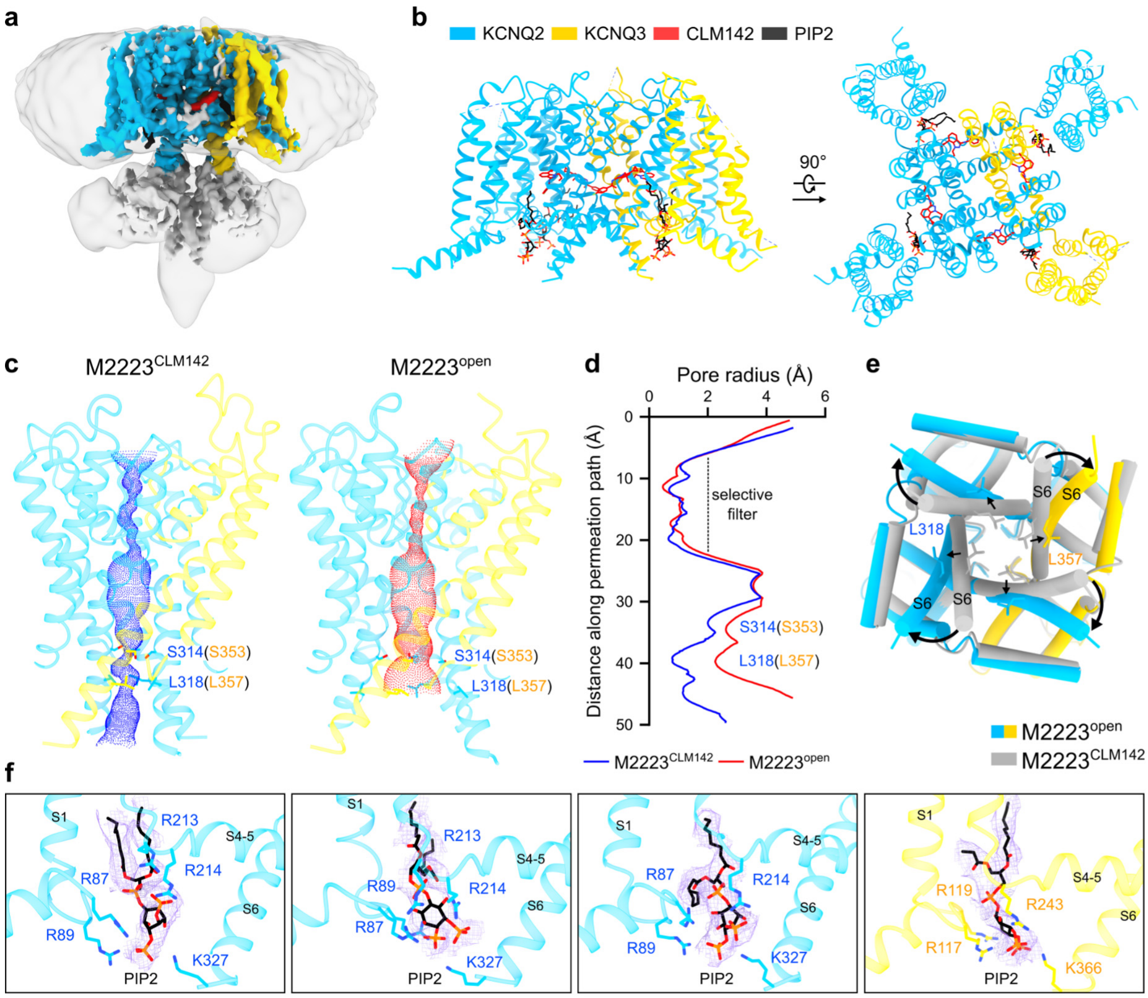

Fig. 6 Structural elucidation of the PIP$_2$-dependent M-channel open state. a Cryo-EM density map of the PIP$_2$-bound open-state M2223 structure. **b** Atomic model of the activated, PIP$_2$-bound open-state M2223 structure, displayed in two orthogonal views. **c** Structural visualization of the pore radius in the closed (CLM142-bound M2223, left) and open (open-state M2223, right) states. Key constriction residues are labeled. **d** Quantitative analysis of the pore radius along the ion permeation pathway for the closed (blue) and open (red) states, confirming gate opening. **e** Conformational changes in the S6 helices during channel activation, highlighting the rearrangement that underlies pore dilation. **f** The PIP$_2$ binding site at the interface of the VSD, S4-S5 linker, and S6 helix. The negatively charged PIP$_2$ headgroup is coordinated by a constellation of basic residues (R87/R117, R89/R119, R213/R242, R214/R243, K327/K366; KCNQ2/KCNQ3 numbering).

the established spatiotemporal expression patterns of KCNQ subunits[12, 16, 38, 70, 71]. During development, KCNQ2 expression stabilizes rapidly while KCNQ3 shows gradual accumulation to its peak levels[16, 38, 70]. Moreover, the relative proportions of KCNQ2 and KCNQ3 expression vary significantly across different brain regions[12, 71, 72]. Such systematic variations in subunit availability would naturally produce different distributions of M-channel assemblies and KCNQ2 homomers, creating a spectrum of channel populations fine-tuned to specific physiological requirements across neuronal circuits and developmental stages.

Despite structural heterogeneity, all four configurations exhibited remarkably similar electrophysiological properties. This surprising functional homogeneity may reflect either: (i) dominant activation by the first responsive subunit as proposed previously, or (ii) limitations in detecting subtle gating differences with current methodologies[73]. If confirmed, such functional equivalence would imply that stoichiometric variation primarily modulates channel density rather than biophysical properties — a possibility that warrants further investigation.

Through chimeric constructs and structural comparison, we established that the KCNQ3 VSD drives the characteristic subthreshold activation of the M-channel. While our structures reveal distinct conformational states for the KCNQ2 and KCNQ3 VSDs, the current local resolution of these peripheral regions limits a definitive atomistic comparison of the entire gating charge pathway. Future high-resolution studies or complementary computational approaches will be necessary to resolve the precise molecular determinants and side-chain interactions that drive these fundamental differences in voltage sensitivity.

Our development of CLM142 addresses the critical need for specific M-channel therapeutics following retigabine's withdrawal[49-52, 54, 55, 57-60, 74, 75]. This optimized compound demonstrates 10-fold greater potency and superior subtype specificity, potentially mitigating the bladder toxicity linked to the non-selective activation of KCNQ1, KCNQ4, and KCNQ5[57]. Notably, the retinal discoloration that prompted retigabine's withdrawal is widely attributed to metabolic liabilities rather than a lack of channel selectivity[60]. While CLM142 achieves the necessary structural specificity to avoid common off-target effects, future clinical development must also address these metabolic risks to ensure long-term safety. Ensuring the success of next-generation activators will require a dual focus on both structural selectivity and metabolic stability.

Our open-state structure suggests that PIP$_2$ mediates VSD-pore coupling through a conserved basic residue interface

(R87/R117, R89/R119, R213/R242, R214/R243, K327/K366), consistent with prior studies[42, 44-46]. Notably, we resolved only a single PIP_2 density per subunit, which matches the P2 site identified in a previous KCNQ4 structure[44]. While the current densities were relatively weak and precluded the identification of additional binding sites, future investigations using PIP_2-incorporated nanodiscs or liposomes may better capture these critical interactions and reveal further mechanistic details. Whether a secondary PIP_2 binding site exists for the heteromeric M-channel remains an important question for future research.

It is worth noting that our findings are subject to several limitations. First, both the structural observations and functional characterizations are based on recombinant proteins expressed in heterologous systems, which may not fully recapitulate the native neuronal environment. Second, the enhanced potency and subtype specificity of CLM142, while rigorously established under patch-clamp conditions, require further validation in physiological disease models and clinical studies to substantiate its therapeutic superiority over retigabine.

By elucidating the M-channel's structural principles, we have: (i) reconciled conflicting stoichiometry models through demonstration of expression-dependent assembly, (ii) provided the first structural explanation for subthreshold activation, and (iii) developed CLM142 as a precision therapeutic candidate. These advances establish a framework for understanding M-channel physiology and developing targeted treatments for epilepsy and related disorders.

MATERIALS AND METHODS

Cell culture and transient transfection

Baculovirus was generated using Sf9 insect cells cultured in Sf900-II SFM medium (GIBCO) at 28 °C. Recombinant proteins were expressed in HEK293F cells maintained in SMM 293-T II serum-free medium (Sino Biological) at 37 °C in a humidified incubator with 5% CO_2. Cells were infected when the density reached 2.0–3.0 × 10^6 cells/mL. HEK293T and CHO-K1 cells were used for electrophysiological recordings. Whole-cell patch-clamp recordings of the engineered concatemers and chimeric constructs were performed using HEK293T cells. To provide microscopic gating insights and cross-validate the whole-cell findings, single-channel recordings were conducted using CHO-K1 cells. Additionally, all pharmacological assays evaluating the effects of the activators CLM142 and retigabine were performed in the CHO-K1 expression system. Both cell lines yielded highly consistent results, ensuring the robustness and reproducibility of the functional data across different mammalian expression environments. HEK293T cells were cultured in Dulbecco's Modified Eagle Medium (DMEM; BI) supplemented with 4.5 mg/mL glucose and 10% (v/v) fetal bovine serum (FBS; BI). CHO-K1 cells were maintained in DMEM/F12 medium (Gibco) supplemented with 10% FBS and 1% (v/v) penicillin–streptomycin (Gibco). All mammalian cells were incubated at 37 °C in a 5% CO_2 atmosphere. Plasmids were transfected when the cells reached ~70% confluency. HEK293T or CHO-K1 cells were transiently transfected with 2.5 µg plasmid DNA per well using Lipofectamine 3000 (Invitrogen) following the manufacturer's instructions.

Cloning, expression, and purification of M-Channel

Gene encoding human KCNQ2 (UniProt: O43526) and KCNQ3 (UniProt: O43525) were synthesized by GENEWIZ and confirmed by sequencing. Full-length sequences of KCNQ2 and KCNQ3 were cloned into a pEGBacMam expression vector with an N-terminal 8×His-GFP-tag and FLAG-tag, respectively[76]. Expression products of the two plasmids were NHis-GFP-KCNQ2 (WT) and NFlag-KCNQ3 (WT). To improve stability and increase production, amino acids (353–533 AA) between HA and HB of the truncated KCNQ2 (64–674 AA) were replaced by a GS-linker (GGGSGGGS); KCNQ3 was also truncated and kept the 93–691AA. Structures, including *apo*, CLM142-bound, and open-state M-channels, were obtained using plasmids engineered as described above. All plasmids were confirmed by DNA sequencing.

To express M-channels, recombinant baculoviruses were generated using the Bac-to-Bac system (ThermoFisher Scientific) as previously described[76]. When cell density reached approximately 2.5 × 10^6 cells/mL, P2 viruses of KCNQ2 and KCNQ3 were co-infected into the cells at a ratio of 1:10 (v/v). After 8 h of culturing, 10 mM sodium butyrate (Sigma) was added to the medium to boost protein expression at 30 °C. Cells were harvested after ~48 h of culturing and frozen in liquid nitrogen before being stored in a −80 °C refrigerator for future use.

For the purification of the M-channel, 6 L cells were solubilized in extraction buffer containing 20 mM Tris-HCl, pH 8.0, 200 mM KCl, 1% DDM/CHS (10:1, w/w; Anatrace), 2 µM leupeptin, 1 µM pepstatin A, 1 µg/mL aprotinin, 1 mM PMSF for 2 h at 4 °C. Solubilized cell lysis were clarified by centrifugation at 13,000 rpm for 1 h. The resulting supernatant was applied to Anti-Flag G1 Affinity Resin (GenScript), and the loaded resin was washed with wash buffer containing 20 mM Tris-HCl pH 8.0, 200 mM KCl, 1mM PMSF and 0.03% GDN (Anatrace). The protein was eluted with 200 µg/mL FLAG peptide in wash buffer and then loaded onto High Affinity Ni-Charged Resin (QIAGEN). The resin was washed with wash buffer supplemented with 30 mM imidazole, and the protein was eluted with 300 mM imidazole. The eluent was concentrated with a 100 kDa MWCO Amicon Ultra-4 centrifugal filter (Millipore) and then applied to size-exclusion chromatography (Superose 6 Increase, 10/300 GL, GE Healthcare) in buffer containing 20 mM Tris-HCl pH 8.0, 150 mM KCl, 1mM PMSF and 0.03% GDN. The peak fractions containing the KCNQ2/KCNQ3 complex were concentrated to about 12 mg/mL for further experiments. To prepare the sample of the M-channel with CLM142, concentrated protein was incubated with 1 mM CLM142 for at least 30 min at 4 °C prior to cryo-EM sample preparation. To obtain the open conformation of the M-channel, the purified protein was incubated with 1 mM PIP_2 and 1mM CLM142. CLM142 was synthesized by the laboratory of Professor Huaiyu Yang (East China Normal University). The PIP_2 we used is 1,2-dioctanoyl-sn-glycero-3-phospho-(1'-myo-inositol-4',5'-bisphosphate) (ammonium salt) purchased from Avanti.

Cryo-EM sample preparation and data collection

To prepare cryo-EM sample, the concentrated complex mixture (3.5 µL) was placed on glow-discharged holey carbon grids (Quantifoil Au R1.2/1.3), which were blotted for 3.5 s and flash-frozen in liquid ethane cooled by liquid nitrogen with Vitrobot (Mark IV, ThermoFisher Scientific). The grids were loaded onto a 300 kV Titan Krios (ThermoFisher Scientific) equipped with a K3 Summit detector (Gatan) and GIF Quantum energy filter. Automated data collection was performed using EPU software (ThermoFisher Scientific) in super-resolution mode at a nominal magnification of 81,000×, with a slit width of 20 eV on the energy filter. A defocus series ranging from −1.5 μm to −2.0 μm was used. Each stack was exposed for 2.56 s with an exposure time of 0.08 s per frame, resulting in a total of 32 frames per stack and the total dose was approximately 50 $e^-/Å^2$ for each stack. The stacks were motion corrected with MotionCor2 and binned 2-fold, resulting in a pixel size of 1.087 Å/pixel[77]. Meanwhile, dose weighting was performed[78]. The defocus values were estimated with Gctf[79].

Cryo-EM data processing

The data processing workflow for the M-channel is illustrated in Supplementary Figs. S5–S7. All steps were conducted in CryoSPARC v4.6.2[80]. For WT M-channel, a total of 5,393 micrographs were collected. Using the template picker, 5,223,566 particles were automatically selected. After particle extraction, multiple rounds of 2D classification, *ab initio* reconstruction, and heterogeneous refinement were performed, resulting in a dataset of 727,947 selected particles. These particles were subjected to non-uniform refinement with C1 symmetry. To distinguish between the KCNQ2 and KCNQ3 components, non-uniform refinement with C4 symmetry was performed to align the symmetry axis along the *Z*-axis. A new particle stack was subsequently generated via symmetry expansion using C4 symmetry. The expanded dataset was classified into two distinct VSD states through multiple rounds of 3D classification, using a focused mask on the VSD region. Particles corresponding to each state were grouped based on their stoichiometric ratios by intersecting different VSD classifications. The resulting particle stacks were further processed using heterogeneous refinement followed by non-uniform refinement to enhance map quality and improve resolution. A total of 16,214, 15,162, and 27,141 micrographs were collected for *apo*, CLM142-bound, and open-state M-channels, respectively. Two strategies were applied for the data processing. The first one followed the same procedure as described for the WT M-channel. The second conducted 3D classification using four separate masks, each enclosing an individual VSD domain. Particles of identical stoichiometries were combined and refined via non-uniform refinement. CryoSieve was used to exclude unwanted particles[81]. The resolution was estimated with the gold-standard Fourier shell correlation 0.143 criterion with high resolution noise substitution[82, 83].

Model building and structure refinement

The AlphaFold-predicted models of KCNQ3 (AlphaFold DB ID: O43525) and KCNQ2 (AlphaFold DB ID: O43526) were initially docked into the final cryo-EM density maps using UCSF ChimeraX[84-86]. Manual model building and adjustment were subsequently performed in Coot v0.9.8.1, with careful attention to the chemical properties of individual amino acid residues[87]. Due to insufficient electron density, the N-terminal and C-terminal regions were not modeled. Several putative lipid molecules were tentatively placed into the observed densities.

Real-space refinement was performed using phenix.real_space_refine in PHENIX 1.20, with secondary structure and geometry restraints applied throughout[88]. To avoid overfitting, gold-standard refinement was employed by alternately refining against one of the two independently calculated half-maps and validating against the other. Final refinement statistics and map quality metrics are summarized in Supplementary Tables S1–S5.

Design of KCNQ2 and KCNQ3 concatemers

Concatemeric constructs were created by the sequential insertion of individual subunits into a pEGBacMam expression vector with an N-terminal 8×His-GFP-tag. Every subunit of KCNQ2 or KCNQ3 was WT without deletions or truncations. Four concatemers were generated: M23, M2333, M2233, and M2223. Adjacent subunits were linked by a GS-linker (GGGGSSGGGGSSGGGGSS). The accuracy of the final sequence was confirmed by both insert digestion and third-generation long-read DNA sequencing.

Quantification of average M-channel stoichiometry

To quantify the average stoichiometry across varying subunit expression levels, we performed systematic transfection experiments using KCNQ2-GFP and KCNQ3 plasmids at molar ratios of 1:1, 1:4, and 1:9 while the total amounts remain constant. Following membrane protein extraction and purification, the resulting heteromeric assemblies were analyzed via size-exclusion chromatography with simultaneous monitoring of total protein concentration (UV absorbance at 280 nm) and KCNQ2 content (GFP fluorescence).

For the quantification of these signals, we utilized the ratio of the relative peak heights. To ensure accuracy, the baseline-corrected maximum height for both the GFP fluorescence and UV absorbance signals was determined at the peak elution volume. The resulting ratio of GFP fluorescence (measured in mV) to UV absorbance (measured in mAu) served as a relative proxy for the average number of KCNQ2 subunits incorporated per assembled tetramer.

Virtual screening and identification of CLM142

To identify novel and selective M-channel activators, we conducted a structure-guided virtual screening campaign using an in-house library comprising over 600 targeted KCNQ channel modulators. Molecular docking was performed by targeting the canonical activator binding pocket, which is structurally defined by the S4-S5 linker, the S5 helix, and the S6 helix of one subunit, along with the S6 helix of the adjacent subunit (Supplementary Fig. S20). Compounds were evaluated and ranked based on their docking scores and predicted binding conformations. Following this virtual screening, the 80 top-ranked candidates were selected for empirical validation using whole-cell patch-clamp electrophysiology. This functional screening successfully identified 9 distinct hit molecules that acted as M-channel agonists. Among these validated hits, compound 7 exhibited the highest potency for channel activation and was subsequently renamed CLM142 for comprehensive structural and pharmacological characterization.

Whole-cell electrophysiology

For the whole-cell electrophysiological experiments of the KCNQ2/KCNQ3 concatemers and chimeric constructs, the whole-cell K^+ currents were recorded in HEK293T cells using an EPC-10 amplifier with Patchmaster 2x92 software (HEKA Elektronik) and glass micropipettes (2.5–4 MΩ) made by P-1000 pipette puller (Sutter Instrument). To record the KCNQ current, the pipette solution contained 100 mM KCl, 50 mM KF, 5 mM EGTA, 10 mM HEPES, adjusted to pH 7.2 with KOH, and the bath contained 130 mM NaCl, 20 mM KCl, 1 mM

$CaCl_2$, 2 mM $MgCl_2$, 5 mM D-Glucose, 10 mM HEPES, adjusted to pH 7.2 with NaOH. Fitmaster 2x92 (HEKA Elektronik) and Prism 10.1.2 (GraphPad Software) were used for data analysis.

To record the currents, a series of 2,000 ms depolarizing steps (holding potential −80 mV) was applied from −90 mV to +80 mV in 10 mV increments. Then, the cells were stimulated by −120 mV for 250 ms to obtain tail currents. The linear component of leak current and capacitive transients was subtracted using the −P/4 procedure, and the voltage errors were minimized using series resistance compensation. The normalized tail current amplitude of the activation curves was plotted against step potentials and fitted by the Boltzmann Sigmoidal function:

$$\frac{I}{I_{max}} = \frac{1}{1+\exp\left(\frac{V_{1/2}-V_m}{k}\right)}$$

Where I refers to the tail current, $V_{1/2}$ refers to the voltage for half-maximal activation, V_m refers to the test potential, and k refers to the slope of the curve. The slope factor (k) derived from the fits is summarized to estimate the apparent gating charge (z_{app}) via the relationship $z_{app} = RT/(F \cdot k)$, where R refers to the gas constant, T refers to the absolute temperature, and F refers to the Faraday constant. The Shapiro-Wilk test and Bartlett's test were used to verify the normality and homogeneity of our data. A one-way ANOVA was employed to assess statistically significant differences between groups.

Whole-cell K^+ currents of the M-channel with CLM142/retigabine were recorded at room temperature using HEKA EPC-10 amplifier on CHO-K1 cells. The series resistance (Rs) was 70–80% compensated using the internal compensation program of the amplifier. The patch pipettes (World Precision Instruments) were pulled to a resistance of 3–5 MΩ. The pipette solution consisted of 140 mM KCl, 3 mM $MgCl_2$, 5 mM EGTA, 5 mM K_2ATP and 10 mM HEPES (pH 7.3, adjusted with KOH, all from Sigma). The extracellular solution contained 145 mM NaCl, 5 mM KCl, 1 mM $CaCl_2$, 3 mM $MgCl_2$, 10 mM D-glucose and 10 mM HEPES (pH 7.3, adjusted with NaOH).

To construct M-channel activation curves with CLM142, cells were held at −80 mV and currents were elicited by a series of 2,000-ms depolarizing steps from −90 mV to +60 mV in 10-mV increments, followed by −120 mV to record tail currents. Activation curves were fitted by the Boltzmann Sigmoidal function. Also, this protocol was used to study the M-channel channel activation kinetics. The M-channel deactivation kinetics were measured by tail currents elicited by a hyperpolarizing voltage of −120 mV for 1,200 ms after a 2,000-ms depolarized potential of +50 mV, with a holding potential of −80 mV. The activation and deactivation traces were fitted to a single exponential function: $I = A \times [1 - \exp(-t/tau)] + I_0$, where I is the current, I_0 is the steady-state amplitude of the current, A is the difference between the peak and steady-state current amplitudes; t is time; and tau is the time constant. The concentration-response curves were analyzed by three parameters logistics regression model. For recordings of KCNQ1, KCNQ4, and KCNQ5 channel currents, pipettes were filled with the intracellular solution of the following composition: 150 mM KCl, 3 mM $MgCl_2$, 5 mM EGTA and 10 mM HEPES (pH 7.3, adjusted with KOH). Extracellular solution contained 145 mM NaCl, 5 mM KCl, 1 mM $CaCl_2$, 3 mM $MgCl_2$ and 10 mM HEPES (pH 7.4, adjusted with NaOH). The methods used to record KCNQ channels were the same as those used to record M-channel currents.

Processed by Clampfit 10.4, patch-clamp data were analyzed in GraphPad Prism 8.0.2. An unpaired two-tailed Student's *t*-test was used to determine significance between groups. n.s. indicates no significance. $*P < 0.05$, $**P < 0.01$, $***P < 0.001$, and $****P < 0.0001$. All data are presented as mean ± SEM.

Inside-out single-channel recordings

Inside-out recordings were performed 48 h after transfection in CHO-K1 cells using EPC10-USB amplifier (HEKA). Patch recordings were digitized at 10 kHz and filtered at 2 kHz. The bath solution contained 175 mM KCl, 4 mM $MgCl_2$, and 10 mM HEPES (pH 7.4, adjusted with KOH). The pipette solution was 150 mM NaCl, 5 mM KCl, 1 mM $MgCl_2$, and 10 mM HEPES (pH 7.4, adjusted with NaOH). The patch pipette was pulled to a resistance of 8–12 MΩ. Single-channel statistical analysis was conducted by Clampfit 10.4 software. All-point histograms were fitted with Gaussian functions to obtain the mean single-channel current (i). Single-channel conductance (γ) was obtained by the equation $\gamma = i/(V - V_E)$, where V is the test potential and V_E is the reversal potential of potassium. The dwell-time histograms were constructed by plotting the logarithm of the dwell times against the square root transformation of the event counts and were fitted with a mixture of two exponential distributions. Events shorter than 2 ms were ignored from analysis.

Synthetic scheme of CLM142

- ***Chemical formula***

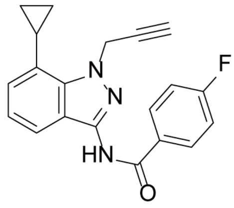

CLM142 (**1**)

- ***Synthetic Route***

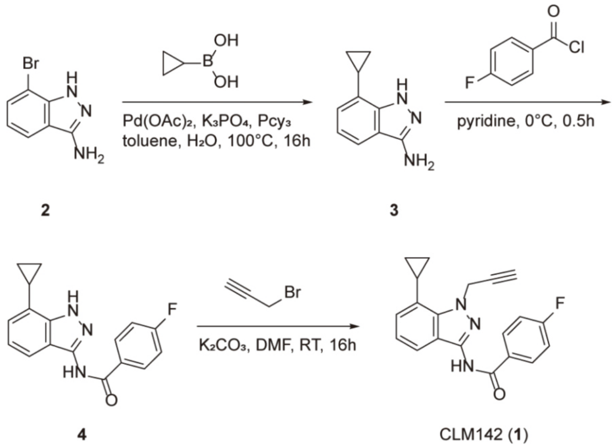

- ***Step 1: 7-cyclopropyl-1H-indazol-3-amine***

7-bromo-1H-indazol-3-amine (**2**, 2.00 g, 9.43 mmol) was dissolved in toluene (20 mL) and water (6 mL). Cyclopropylboronic acid (5.67 g, 66.01 mmol), tricyclohexylphosphine (0.53 g, 1.89 mmol), potassium phosphate (6.01 g, 28.29 mmol) and palladium acetate (0.42 g, 1.89 mmol) were added sequentially. Under nitrogen protection, the mixture was heated to 100 °C and stirred for 16 h. TLC (PE:EA = 1:1, Rf =

0.1) indicated the complete consumption of the starting material. The reaction solution was cooled to room temperature, filtered through Celite, quenched with water (10 mL), and extracted with ethyl acetate (10 mL × 3). The combined organic phases were washed with saturated brine (20 mL × 3), dried over anhydrous sodium sulfate, and concentrated. The crude product was purified by silica gel column chromatography (PE:EA = 2:1–2:3) to afford the title compound **3** as a white solid (0.69 g, yield 42%).

LC-MS: m/z = 174.2 $[M+H]^+$

- ***Step 2: N-(7-cyclopropyl-1H-indazol-3-yl)-4-fluorobenzamide***

Compound **3** (380 mg, 2.19 mmol) was dissolved in pyridine (2 mL), cooled to 0 °C, and 4-fluorobenzoyl chloride (347 mg, 2.19 mmol) was added dropwise. The mixture was stirred at this temperature for 30 min. TLC (PE:EA = 1:1, Rf = 0.4) showed the complete reaction of the starting material. The reaction was quenched with water (10 mL) and extracted with ethyl acetate (10 mL × 3). The combined organic phases were washed with saturated brine (20 mL × 3), dried over anhydrous sodium sulfate, and concentrated. The crude product was purified by silica gel column chromatography (PE:EA = 5:1–2:1) to obtain the title Compound **4** as a brown solid (325 mg, yield 50%).

LC-MS: m/z = 296.1 $[M+H]^+$

- ***Step 3: N-(7-cyclopropyl-1-(prop-2-yn-1-yl)-1H-indazol-3-yl)-4-fluorobenzamide***

Compound **4** (80 mg, 0.27 mmol) was dissolved in N,N-dimethylformamide (2 mL). 3-bromopropyne (39 mg, 0.33 mmol) and potassium carbonate (75 mg, 0.54 mmol) were added at room temperature, and the mixture was stirred at room temperature for 16 h. TLC (PE:EA = 2:1, Rf = 0.4) indicated a small amount of starting material remaining. The reaction was quenched with water (10 mL) and extracted with ethyl acetate (10 mL × 3). The combined organic phases were washed with saturated brine (20 mL × 3), dried over anhydrous sodium sulfate, and concentrated. Purification by preparative HPLC (TFA) gave the title compound CLM142 (**1**) as a white solid (18 mg, yield 20%).

LC-MS: m/z = 334.2 $[M+H]^+$

HPLC:99.10% purity, 220 nm

^{1}HNMR (400 MHz, *DMSO-d6*) δ 10.88 (s, 1H), 8.15 (dd, J = 8.4, 5.6 Hz, 2H), 7.53 (d, J = 8.4 Hz, 1H), 7.39 (t, J = 8.8 Hz, 2H), 7.17 (d, J = 7.2 Hz, 1H), 7.04 (t, J = 8.0 Hz, 1H), 5.56 (d, J = 1.6 Hz, 2H), 3.44 (s, 1H), 2.49-2.44 (m, 1H), 1.10-1.05 (m, 2H), 0.89-0.83 (m, 2H).

DATA AVAILABILITY

Atomic coordinates and EM maps of M-channels reported in this study (WT M2223: 24VL and EMD-69843; WT M2233: 24VM and EMD-69844; WT M2323: 24VN and EMD-69845; WT M2333: 24VO and EMD-69846; Apo M2223 (no symmetry expansion): 24VI and EMD-69840; Apo M2223 (symmetry expansion): 24VP and EMD-69847; Apo M2233: 24VQ and EMD-69848; Apo M2323: 24VR and EMD-69849; Apo M2333: 24VS and EMD-69850; CLM142-bound M2223 (no symmetry expansion): 24VT and EMD-69851; CLM142-bound M2223 (symmetry expansion): 24VJ and EMD-69841; CLM142-bound M2233: 24VU and EMD-69852; CLM142-bound M2323: 24VV and EMD-69853; CLM142-bound M2333: 24VW and EMD-69854; Open-state M2223 (no symmetry expansion): 24VK and EMD-69842; Open-state M2223 (symmetry expansion): 24VX and EMD-69855; Open-state M2233: 24VY and EMD-69856; Open-state M2323: 24VZ and EMD-69857; Open-state M2333: 24WA and EMD-69858) have been deposited in the Protein Data Bank and the Electron Microscopy Data Bank.

ACKNOWLEDGMENTS

We thank the Cryo-EM Facility and the HPC Center of Westlake University for providing data collection and computation support, respectively. We are also thankful for the support of the East China Normal University Multifunctional Platform for Innovation (001). This work was supported by grants from the National Key R&D Program of China (2024YFA0916903 to H.S.), the National Natural Science Foundation of China (82525063 to Huaiyu Y.), the Zhejiang Provincial Natural Science Foundation (DQ24C050001 to H.S.), the Research Center for Industries of the Future (RCIF), Westlake University, the Westlake Education Foundation (to H.S.), and the East China Normal University Medicine and Health Joint Fund (2022JKXYD07001 to Huaiyu Y.).

AUTHOR CONTRIBUTIONS

The project was conceived by H.S. Y.W., Hui Y. and X.L. performed molecular cloning, protein purification, sample preparation, and cryo-EM micrograph collection. Y.Q. carried out cryo-EM data processing, structure determination, and model building. J.L. identified the CLM142 activator and conducted electrophysiological studies on CHO-K1 cells under the supervision of Huaiyu Y. Y.Y. synthesized the CLM142 molecule. W.H. performed electrophysiological characterization of KCNQ2 and KCNQ3 concatemers and chimeras on HEK293T cells under the supervision of K.W. G.X. validated the sequences of KCNQ2 and KCNQ3 concatemers using third-generation sequencing data under the supervision of X.W. All authors contributed to data analysis. H.S. and Huaiyu Y. wrote the manuscript with intellectual input from all authors.

COMPETING INTERESTS

J.L., Y.Y., and Huaiyu Y. are inventors of patent application 202311463618.7 that covers the potential usage of CLM142. The other authors declare no competing interests.

REFERENCES

1. Yang, W.P. et al. Functional expression of two KvLQT1-related potassium channels responsible for an inherited idiopathic epilepsy. *J. Biol. Chem.* **273**, 19419–19423 (1998).
2. Wang, H.S. et al. KCNQ2 and KCNQ3 potassium channel subunits: molecular correlates of the M-channel. *Science* **282**, 1890–1893 (1998).
3. Schroeder, B.C., Kubisch, C., Stein, V. & Jentsch, T.J. Moderate loss of function of cyclic-AMP-modulated KCNQ2/KCNQ3 K^+ channels causes epilepsy. *Nature* **396**, 687–690 (1998).
4. Brown, D.A. & Adams, P.R. Muscarinic suppression of a novel voltage-sensitive K^+ current in a vertebrate neurone. *Nature* **283**, 673–676 (1980).
5. Jentsch, T.J. Neuronal KCNQ potassium channels: physiology and role in disease. *Nat. Rev. Neurosci.* **1**, 21–30 (2000).
6. Maljevic, S., Wuttke, T.V. & Lerche, H. Nervous system K_V7 disorders: breakdown of a subthreshold brake. *J. Physiol.* **586**, 1791–1801 (2008).
7. Marrion, N.V. Control of M-current. *Annu. Rev. Physiol.* **59**, 483–504 (1997).
8. Delmas, P. & Brown, D.A. Pathways modulating neural KCNQ/M (Kv7) potassium channels. *Nat. Rev. Neurosci.* **6**, 850–862 (2005).
9. Greene, D.L. & Hoshi, N. Modulation of Kv7 channels and excitability in the brain. *Cell. Mol. Life Sci.* **74**, 495–508 (2017).

10. Bean, B.P. The action potential in mammalian central neurons. *Nat. Rev. Neurosci.* **8**, 451–465 (2007).
11. Yue, C.Y. & Yaari, Y. KCNQ/M channels control spike afterdepolarization and burst generation in hippocampal neurons. *J. Neurosci.* **24**, 4614–4624 (2004).
12. Cooper, E.C. et al. Colocalization and coassembly of two human brain M-type potassium channel subunits that are mutated in epilepsy. *Proc. Natl. Acad. Sci. USA* **97**, 4914–4919 (2000).
13. Singh, N.A. et al. A novel potassium channel gene, *KCNQ2*, is mutated in an inherited epilepsy of newborns. *Nat. Genet.* **18**, 25–29 (1998).
14. Biervert, C. et al. A potassium channel mutation in neonatal human epilepsy. *Science* **279**, 403–406 (1998).
15. Charlier, C. et al. A pore mutation in a novel KQT-like potassium channel gene in an idiopathic epilepsy family. *Nat. Genet.* **18**, 53–55 (1998).
16. Tinel, N., Lauritzen, I., Chouabe, C., Lazdunski, M. & Borsotto, M. The KCNQ2 potassium channel: splice variants, functional and developmental expression. Brain localization and comparison with KCNQ3. *FEBS Lett.* **438**, 171–176 (1998).
17. Schwake, M., Pusch, M., Kharkovets, T. & Jentsch, T.J. Surface expression and single channel properties of KCNQ2/KCNQ3, M-type K^+ channels involved in epilepsy. *J. Biol. Chem.* **275**, 13343–13348 (2000).
18. Grinton, B.E. et al. Familial neonatal seizures in 36 families: clinical and genetic features correlate with outcome. *Epilepsia* **56**, 1071–1080 (2015).
19. Zara, F. et al. Genetic testing in benign familial epilepsies of the first year of life: clinical and diagnostic significance. *Epilepsia* **54**, 425–436 (2013).
20. Dedek, K. et al. Myokymia and neonatal epilepsy caused by a mutation in the voltage sensor of the KCNQ2 K^+ channel. *Proc. Natl. Acad. Sci. USA* **98**, 12272–12277 (2001).
21. Singh, N.A. et al. *KCNQ2* and *KCNQ3* potassium channel genes in benign familial neonatal convulsions: expansion of the functional and mutation spectrum. *Brain* **126**, 2726–2737 (2003).
22. Trump, N. et al. Improving diagnosis and broadening the phenotypes in early-onset seizure and severe developmental delay disorders through gene panel analysis. *J. Med. Genet.* **53**, 310–317 (2016).
23. del Giudice, E.M. et al. Benign familial neonatal convulsions (BFNC) resulting from mutation of the *KCNQ2* voltage sensor. *Eur. J. Hum. Genet.* **8**, 994–997 (2000).
24. Surti, T.S., Huang, L., Jan, Y.N., Jan, L.Y. & Cooper, E.C. Identification by mass spectrometry and functional characterization of two phosphorylation sites of KCNQ2/KCNQ3 channels. *Proc. Natl. Acad. Sci. USA* **102**, 17828–17833 (2005).
25. Hirose, S. et al. A novel mutation of *KCNQ3* (c.925T→C) in a Japanese family with benign familial neonatal convulsions. *Ann. Neurol.* **47**, 822–826 (2000).
26. Miceli, F., Soldovieri, M.V., Weckhuysen, S., Cooper, E. & Taglialatela, M. KCNQ2-Related Disorders. 2010 Apr 27 [Updated 2022 May 19]. In: Adam MP, Feldman J, Mirzaa GM, et al., editors. GeneReviews® [Internet]. Seattle (WA): University of Washington, Seattle; 1993-2024.
27. Weckhuysen, S. et al. *KCNQ2* encephalopathy: emerging phenotype of a neonatal epileptic encephalopathy. *Ann. Neurol.* **71**, 15–25 (2012).
28. Dimassi, S. et al. Whole-exome sequencing improves the diagnosis yield in sporadic infantile spasm syndrome. *Clin. Genet.* **89**, 198–204 (2016).
29. Borgatti, R. et al. A novel mutation in KCNQ2 associated with BFNC, drug resistant epilepsy, and mental retardation. *Neurology* **63**, 57–65 (2004).
30. Kato, M. et al. Clinical spectrum of early onset epileptic encephalopathies caused by *KCNQ2* mutation. *Epilepsia* **54**, 1282–1287 (2013).
31. Syrbe, S. et al. *De novo* loss- or gain-of-function mutations in *KCNA2* cause epileptic encephalopathy. *Nat. Genet.* **47**, 393–399 (2015).
32. Nissenkorn, A. et al. Donepezil as a new therapeutic potential in KCNQ2- and KCNQ3-related autism. *Front. Cell. Neurosci.* **18**, 1380442 (2024).
33. Siracusano, M., Marcovecchio, C., Riccioni, A., Dante, C. & Mazzone, L. Autism spectrum disorder and a De Novo Kcnq2 gene mutation: a case report. *Pediatr. Rep.* **14**, 200–206 (2022).
34. Springer, K., Varghese, N. & Tzingounis, A.V. Flexible stoichiometry: implications for KCNQ2- and KCNQ3-associated neurodevelopmental disorders. *Dev. Neurosci.* **43**, 191–200 (2021).
35. Sands, T.T. et al. Autism and developmental disability caused by *KCNQ3* gain-of-function variants. *Ann. Neurol.* **86**, 181–192 (2019).
36. Surti, T.S. & Jan, L.Y. A potassium channel, the M-channel, as a therapeutic target. *Curr. Opin. Investig. Drugs* **6**, 704–711 (2005).
37. Li, X.X. et al. Molecular basis for ligand activation of the human KCNQ2 channel. *Cell Res.* **31**, 52–61 (2021).
38. Hadley, J.K. et al. Stoichiometry of expressed KCNQ2/KCNQ3 potassium channels and subunit composition of native ganglionic M channels deduced from block by tetraethylammonium. *J. Neurosci.* **23**, 5012–5019 (2003).
39. Stewart, A.P. et al. The Kv7.2/Kv7.3 heterotetramer assembles with a random subunit arrangement. *J. Biol. Chem.* **287**, 11870–11877 (2012).
40. Shapiro, M.S. et al. Reconstitution of muscarinic modulation of the KCNQ2/KCNQ3 K^+ channels that underlie the neuronal M current. *J. Neurosci.* **20**, 1710–1721 (2000).
41. Sun, J. & MacKinnon, R. Cryo-EM structure of a KCNQ1/CaM complex reveals insights into congenital long QT syndrome. *Cell* **169**, 1042–1050.e9 (2017).
42. Sun, J. & MacKinnon, R. Structural basis of human KCNQ1 modulation and gating. *Cell* **180**, 340–347.e9 (2020).
43. Li, T. et al. Structural basis for the modulation of human KCNQ4 by small-molecule drugs. *Mol. Cell* **81**, 25–37.e4 (2021).
44. Zheng, Y. et al. Structural insights into the lipid and ligand regulation of a human neuronal KCNQ channel. *Neuron* **110**, 237–247.e4 (2022).
45. Yang, Z.N. et al. Phosphatidylinositol 4,5-bisphosphate activation mechanism of human KCNQ5. *Proc. Natl. Acad. Sci. USA* **122**, e2416738122 (2025).
46. Zhang, S.Y. et al. A small-molecule activation mechanism that directly opens the KCNQ2 channel. *Nat. Chem. Biol.* **20**, 847–856 (2024).
47. Yang, N.D. et al. Electro-mechanical coupling of KCNQ channels is a target of epilepsy-associated mutations and retigabine. *Sci. Adv.* **8**, eabo3625 (2022).
48. Telezhkin, V., Brown, D.A. & Gibb, A.J. Distinct subunit contributions to the activation of M-type potassium channels by $PI(4,5)P_2$. *J. Gen. Physiol.* **140**, 41–53 (2012).
49. Liu, Y.N., Bian, X.L. & Wang, K.W. Pharmacological activation of neuronal voltage-gated Kv7/KCNQ/M-channels for potential therapy of epilepsy and pain. In: Gamper, N. & Wang, K.W. eds. Pharmacology of potassium channels. Cham: Springer, 231–251 (2021).
50. Barrese, V., Stott, J.B. & Greenwood, I.A. KCNQ-encoded potassium channels as therapeutic targets. *Annu. Rev. Pharmacol. Toxicol.* **58**, 625–648 (2018).
51. Gunthorpe, M.J., Large, C.H. & Sankar, R. The mechanism of action of retigabine (ezogabine), a first-in-class K^+ channel opener for the treatment of epilepsy. *Epilepsia* **53**, 412–424 (2012).
52. Tatulian, L., Delmas, P., Abogadie, F.C. & Brown, D.A. Activation of expressed KCNQ potassium currents and native neuronal M-type potassium currents by the anti-convulsant drug retigabine. *J. Neurosci.* **21**, 5535–5545 (2001).
53. Linley, J.E., Pettinger, L., Huang, D.Y. & Gamper, N. M channel enhancers and physiological M channel block. *J. Physiol.* **590**, 793–807 (2012).
54. Porter, R.J., Nohria, V. & Rundfeldt, C. Retigabine. *Neurotherapeutics* **4**, 149–154 (2007).
55. French, J.A. et al. Randomized, double-blind, placebo-controlled trial of ezogabine (retigabine) in partial epilepsy. *Neurology* **76**, 1555–1563 (2011).
56. Rundfeldt, C. The new anticonvulsant retigabine (D-23129) acts as an opener of K^+ channels in neuronal cells. *Eur. J. Pharmacol.* **336**, 243–249 (1997).
57. Brickel, N., Gandhi, P., VanLandingham, K., Hammond, J. & DeRossett, S. The urinary safety profile and secondary renal effects of retigabine (ezogabine): a first-in-class antiepileptic drug that targets KCNQ (K_v7) potassium channels. *Epilepsia* **53**, 606–612 (2012).
58. Daniluk, J., Cooper, J.A., Stender, M. & Kowalczyk, A. Survey of physicians' understanding of specific risks associated with retigabine. *Drugs Real World Outcomes* **3**, 155–163 (2016).
59. Faulkner, M.A. & Burke, R.A. Safety profile of two novel antiepileptic agents approved for the treatment of refractory partial seizures: ezogabine (retigabine) and perampanel. *Expert Opin. Drug Saf.* **12**, 847–855 (2013).
60. Groseclose, M.R. & Castellino, S. An investigation into retigabine (ezogabine) associated dyspigmentation in rat eyes by MALDI imaging mass spectrometry.

Chem. Res. Toxicol. **32**, 294–303 (2019).
61. Jiang, Y.X. et al. X-ray structure of a voltage-dependent K$^+$ channel. *Nature* **423**, 33–41 (2003).
62. Schwake, M. et al. Structural determinants of M-type KCNQ (K$_V$7) K$^+$ channel assembly. *J. Neurosci.* **26**, 3757–3766 (2006).
63. Schwake, M., Jentsch, T.J. & Friedrich, T. A carboxy-terminal domain determines the subunit specificity of KCNQ K$^+$ channel assembly. *EMBO Rep.* **4**, 76–81 (2003).
64. Tao, X., Lee, A., Limapichat, W., Dougherty, D.A. & MacKinnon, R. A gating charge transfer center in voltage sensors. *Science* **328**, 67–73 (2010).
65. Zhang, X. & Yan, N.E. The conformational shifts of the voltage sensing domains between Na$_V$Rh and Na$_V$Ab. *Cell Res.* **23**, 444–447 (2013).
66. Zaydman, M.A. & Cui, J.M. PIP$_2$ regulation of KCNQ channels: biophysical and molecular mechanisms for lipid modulation of voltage-dependent gating. *Front. Physiol.* **5**, 195 (2014).
67. Li, Y., Gamper, N., Hilgemann, D.W. & Shapiro, M.S. Regulation of Kv7 (KCNQ) K$^+$ channel open probability by phosphatidylinositol 4,5-bisphosphate. *J. Neurosci.* **25**, 9825–9835 (2005).
68. Zaydman, M.A. et al. Kv7.1 ion channels require a lipid to couple voltage sensing to pore opening. *Proc. Natl. Acad. Sci. USA* **110**, 13180–13185 (2013).
69. Li, J.N. et al. Small molecule inhibits KCNQ channels with a non-blocking mechanism. *Nat. Chem. Biol.* **21**, 1100–1109 (2025).
70. Dirkx, N., Miceli, F., Taglialatela, M. & Weckhuysen, S. The role of Kv7.2 in neurodevelopment: insights and gaps in our understanding. *Front. Physiol.* **11**, 570588 (2020).
71. Kanaumi, T. et al. Developmental changes in KCNQ2 and KCNQ3 expression in human brain: possible contribution to the age-dependent etiology of benign familial neonatal convulsions. *Brain Dev.* **30**, 362–369 (2008).
72. Klinger, F., Gould, G., Boehm, S. & Shapiro, M.S. Distribution of M-channel subunits KCNQ2 and KCNQ3 in rat hippocampus. *NeuroImage* **58**, 761–769 (2011).
73. Osteen, J.D. et al. Allosteric gating mechanism underlies the flexible gating of KCNQ1 potassium channels. *Proc. Natl. Acad. Sci. USA* **109**, 7103–7108 (2012).
74. Zahra, A., Liu, R., Wang, J.J. & Wu, J.P. Identifying the mechanism of action of the Kv7 channel opener, retigabine in the treatment of epilepsy. *Neurol. Sci.* **44**, 3819–3825 (2023).
75. Orhan, G., Wuttke, T.V., Nies, A.T., Schwab, M. & Lerche, H. Retigabine/Ezogabine, a KCNQ/K$_V$7 channel opener: pharmacological and clinical data. *Expert Opin. Pharmacother.* **13**, 1807–1816 (2012).
76. Goehring, A. et al. Screening and large-scale expression of membrane proteins in mammalian cells for structural studies. *Nat. Protoc.* **9**, 2574–2585 (2014).
77. Zheng, S.Q. et al. MotionCor2: anisotropic correction of beam-induced motion for improved cryo-electron microscopy. *Nat. Methods* **14**, 331–332 (2017).
78. Grant, T. & Grigorieff, N. Measuring the optimal exposure for single particle cryo-EM using a 2.6 Å reconstruction of rotavirus VP6. *ELife* **4**, e06980 (2015).
79. Zhang, K. Gctf: real-time CTF determination and correction. *J. Struct. Biol.* **193**, 1–12 (2016).
80. Punjani, A., Rubinstein, J.L., Fleet, D.J. & Brubaker, M.A. cryoSPARC: algorithms for rapid unsupervised cryo-EM structure determination. *Nat. Methods* **14**, 290–296 (2017).
81. Zhu, J.Y. et al. A minority of final stacks yields superior amplitude in single-particle cryo-EM. *Nat. Commun.* **14**, 7822 (2023).
82. Rosenthal, P.B. & Henderson, R. Optimal determination of particle orientation, absolute hand, and contrast loss in single-particle electron cryomicroscopy. *J. Mol. Biol.* **333**, 721–745 (2003).
83. Chen, S.X. et al. High-resolution noise substitution to measure overfitting and validate resolution in 3D structure determination by single particle electron cryomicroscopy. *Ultramicroscopy* **135**, 24–35 (2013).
84. Varadi, M. et al. AlphaFold protein structure database in 2024: providing structure coverage for over 214 million protein sequences. *Nucleic Acids Res.* **52**, D368–D375 (2024).
85. Jumper, J. et al. Highly accurate protein structure prediction with AlphaFold. *Nature* **596**, 583–589 (2021).
86. Pettersen, E.F. et al. UCSF ChimeraX: structure visualization for researchers, educators, and developers. *Protein Sci.* **30**, 70–82 (2021).
87. Emsley, P., Lohkamp, B., Scott, W.G. & Cowtan, K. Features and development of *Coot*. *Acta Crystallogr. D Biol. Crystallogr.* **66**, 486–501 (2010).
88. Adams, P.D. et al. *PHENIX*: a comprehensive Python-based system for macromolecular structure solution. *Acta Crystallogr. D Biol. Crystallogr.* **66**, 213–221 (2010).
89. Madeira, F. et al. The EMBL-EBI job dispatcher sequence analysis tools framework in 2024. *Nucleic Acids Res.* **52**, W521–W525 (2024).
90. Robert, X. & Gouet, P. Deciphering key features in protein structures with the new ENDscript server. *Nucleic Acids Res.* **42**, W320–W324 (2014).

ADDITIONAL INFORMATION

Supplementary information The online version contains supplementary material available at https://doi.org/10.15302/vita.2026.05.0032.

Correspondence and requests for materials should be addressed to Huaiyu Yang or Huaizong Shen.

Reprints and permission information is available at https://www.vita-journal.com/.